Assessing the Impact of Sun Glint on Seagrass and Benthic Habitat Classification Accuracy across various Algorithms using PlanetScope Imagery

Margaux Angelica Cruz [1]

[1] Department of Geodetic Engineering, University of the Philippines Diliman, Quezon City, Philippines - macruz4@up.edu.ph

Keywords: Seagrass, Benthic Classification, Image Quality, PlanetScope, Sun Glint, SDG.

Abstract

Seagrasses are ecologically important yet highly threatened blue carbon ecosystems that play a critical role in environmental protection, biodiversity conservation, and carbon sequestration. However, their spatial heterogeneity and dynamic temporal behavior pose challenges to accurate mapping and long-term monitoring. The availability of publicly accessible satellite images with high spatial and temporal resolution, and advances in machine learning, have gradually expanded seagrass geospatial research and led to more accurate and robust image classifications. This study evaluated the performance of traditional and machine learning methods for seagrass and benthic habitat mapping using clear and sun-glinted 3-meter resolution PlanetScope imagery. Classification accuracy metrics were compared across multiple algorithms and varying image quality, using two different reference datasets. Results indicated that the Maximum Likelihood Classification and Support Vector Machine Classification achieved the highest overall accuracy and kappa statistics for the clearest image used, the 8-band PlanetScope image acquired on February 16. As expected, the application of the sun glint correction procedure improved classification accuracies for lower-quality images, particularly for the Random Forest Classification, which showed consistent and pronounced gains after deglinting. These findings demonstrate the potential of PlanetScope images for seagrass and benthic mapping, keeping in mind that careful image selection remains essential due to the imagery’s inherent sensitivity to sun glint and other radiometric inconsistencies affecting classification performance. In the absence of optimal or clear images, scenes with lower image quality may still be effectively utilized with the application of radiometric correction procedures such as sun glint removal.

1. Introduction

1.1 Background and Significance

Seagrasses are benthic habitats that play a crucial role in environmental protection, biodiversity conservation, and carbon sequestration (Cullen-Unsworth and Unsworth, 2013) and (United Nations Environment Programme, 2020). Seagrass meadows are proven to be capable of providing coastal protection from flooding and erosion (Ondiviela et al., 2014). They also contribute to the improvement of water quality by means of natural filtration, oxygenation, and removal of excess nutrients and bacteria from the water (de los Santos et al., 2020). These unassuming benthic habitats have significant contributions to meeting our sustainable SDG 13 (Climate Action) and SDG 14 (Life Below Water).

Like most natural habitats, seagrasses face threats that necessitate appropriate action towards their protection and rehabilitation (de Fouw et al., 2024), (Sievers et al., 2019) and (Unsworth et al., 2018). Anthropogenic activities such as coastal development, mining, and pollution-causing activities lead to the degradation or loss of expansive seagrass areas. Over 80 years, the rate of decline has accelerated, with a total loss of 35% after 1980 (Waycott et al., 2009). There have been various efforts to help protect benthic habitat, both globally and locally, such as the designation of marine protected areas (MPA). The World Database of Protected Areas (WDPA) lists a total of 16,539 MPAs all over the world, covering only 9.61% of the oceans globally. Marine habitat conservation entails regular monitoring, traditionally using field surveys such as transects, quadrats, snorkelling or diving, and underwater video tows. Remote sensing offers an efficient, consistent, and economical solution to mapping and monitoring large areas over several time periods (Hedley et al., 2016). It has been proven to be an effective tool in mapping benthic habitats, including seagrass, globally at various scales (Bremner et al., 2023) and (Kutser et al., 2020).

The numerous ecosystem services provided by seagrasses and the threat to their existence necessitates targeted and timely monitoring. Several studies to map seagrass extent over the years have been done using moderate spatial resolution satellite images such as the 30-m Landsat and the 10-m Sentinel-2. Although the usefulness of such satellite images has been proven for seagrass mapping (Hossain et al., 2015), (Li et al., 2023) and (Veettil et al., 2020), challenges arise due to the seasonality and fragmented spatial distribution of seagrass areas (Zoffoli et al., 2020). Moreover, in tropical countries like the Philippines, the persistence of cloud cover in satellite images poses an additional challenge in the timely and regular monitoring of seagrass habitats. The revisit frequency of moderate-resolution satellites may not be able to yield enough usable images for such studies.

The advent of higher resolution images in recent years has led to a wider range of prospects for mapping small-scale habitats such as seagrasses. It is now possible to detect small patches or narrow strips of seagrass areas using high resolution imagery such as Ikonos, Quickbird, Worldview-2, and Worldview-3 (Baumstark et al., 2016). The use of high-resolution satellite images led to improved mapping accuracies compared to medium resolution images (Mederos-Barrera et al., 2022) and (Pu and Bell, 2017). However, the high cost and low accessibility of these images pose limitations in studying other areas or for more frequent mapping requirements.

This research uses high resolution PlanetScope images to classify seagrass and benthic habitat for a study area in the Philippines. The access to these satellite images with high spatial and temporal resolution, through the Education and Research Program, capacitates more detailed research worldwide. Studies have shown the potential of PlanetScope images for mapping benthic habitat, including seagrass areas (Wicaksono and Lazuardi, 2018). However, despite the spatial and temporal advantage of PlanetScope images, there are certain limitations that need to be considered due to image quality inconsistencies due to noise, sun glint, and radiometric variations (Wicaksono et al., 2023). The daily revisit time of the satellite may be able to compensate for this limitation by enabling the selection of higher-quality images within the required time period. In the absence of clear images, however, it will be useful to explore how the previously mentioned issues in image quality will affect image classification results and in what ways these can be minimized. In this study, the effect of sun glint and sun glint correction in the accuracies of classified PlanetScope images was investigated using accuracy metrics.

1.2 Objectives and Scope

This study aimed to assess the impact of image quality on the image classification of seagrass and other general benthic habitat using both traditional and machine learning supervised classification algorithms. Resulting accuracies using the original 3-meter resolution PlanetScope images versus the sun glint corrected images were compared across classifiers. The robustness of the Maximum Likelihood (ML), Random Forest (RF), and Support Vector Machine (SVM) classification methods to varying levels of image quality was quantified using overall accuracies and kappa statistics. The goal was to investigate whether there will be gains in classification accuracy after applying a simple sun glint correction method. Moreover, a comparative analysis of the three classifiers in terms of consistent and good performance was implemented.

2. Methodology

2.1 Study Area

The seagrass area is in San Salvador Island, Masinloc, Zambales (Fig. 1) in the north-western coast of the Philippines. It is a 4.62 km^2 island inhabited by a population of 2,544 people based on the Year 2020 Philippine Census. The island is surrounded by benthic habitat composed of seagrass, seaweed, corals. The entire island is within the 75.58 km^2 Masinloc and Oyon Bay Protected Landscape and Seascape, a protected area designated through the Republic Act No. 11038 or the Expanded National Integrated Protected Areas System Act of 2018 (E-NIPAS 2018). About 3 kilometers north of the island is the coal-fired Masinloc Power Plant, which started operations in 1998 and further expanded its capacity in 2020.

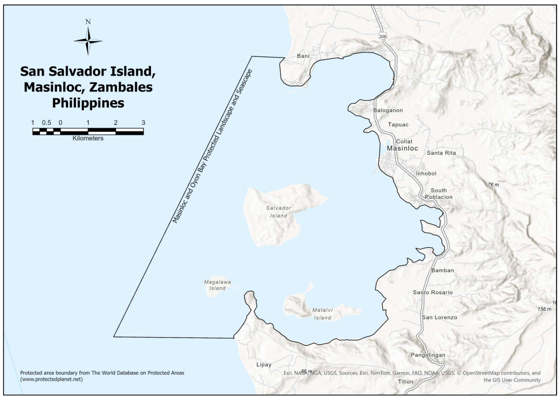

Figure 1. The study area and its surrounding protected area.

2.2 Data and Methods

The PlanetScope constellation operated by Planet Labs consists of 130 CubeSat satellites with the capability to capture images of the entire globe daily. The Dove Classic instrument of PlanetScope has been capturing 4-band images of the world at a spatial resolution of 3 meters x 3 meters for almost 10 years since July 2014. On 29 April 2022, the SuperDove 8-band product made way for more applications using the additional spectral information. Table 1 shows the 8 spectral bands and a brief description of each band. PlanetScope satellite images acquired on 16 February 2025, 01 May 2025, and 02 May 2025 were downloaded from the Planet Explorer using the Search and Order tool. These orthorectified Level 3B products are expressed in scaled surface reflectance (SR), which represents the amount of light reflected by the Earth’s surface. Image processing and analysis were performed using ArcGIS Pro 3.4.

Band Number	Band Name	Wavelength
Band 1	Coastal Blue	431 – 452 nm
Band 2	Blue	465 – 515 nm
Band 3	Green I	513 – 549 nm
Band 4	Green	547 – 583 nm
Band 5	Yellow	600 – 620 nm
Band 6	Red	650 – 680 nm
Band 7	Red Edge	697 – 713 nm
Band 8	Near Infrared	845 – 885 nm

Table 1. PlanetScope’s eight spectral bands and description (Planet Team, 2025).

The entire process, from image acquisition to validation, is illustrated in Figure 2. The first group describes the image acquisition and preprocessing steps, which includes the sun glint correction. The second group illustrates the processes taken for training, classification, and accuracy assessment.

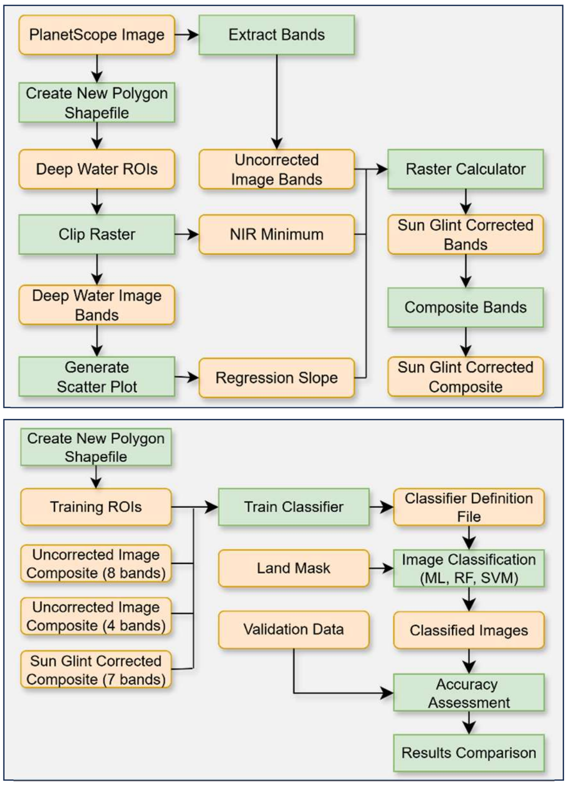

Figure 2. Detailed methodology.

2.3 Sun Glint Correction

Radiometric and geometric correction were not required for the downloaded images, being all Level 3B SR scenes. However, inconsistencies in radiometric quality of PlanetScope images, such as the appearance of noisy pixels or image artifacts, sun glint, and surface waves, impose certain limitations on its use. In particular, the presence of sun glint and surface wave patterns in the image scenes used in this study posed image quality issues that may affect image classification. Prior to testing various image classification algorithms, a sun glint correction or deglinting method was performed to try improving image quality and classification accuracies. The method by Hedley et al., 2005 is a simple but robust method that uses the linear regression parameters from the visible and NIR bands to correct each of the pixel values. The equation used to derive sun glint-corrected bands using this method is shown in Equation 1.

$$R_i' = R_i - b_i(R_{NIR} - MIN_{NIR}) \tag{1}$$

where $R_i' = sunglint\ corrected\ pixel\ value\ in\ band\ i$
$R_i = original\ pixel\ value\ in\ band\ i$
$b_i = regression\ slope$
$R_{NIR} = original\ pixel\ value\ in\ NIR\ band$
$MIN_{NIR} = minimum\ sample\ pixel\ value\ in\ NIR\ band$

Regions of interest (ROIs) were drawn over the deep-water areas containing a range of sun glint effects. Aside from using the spectral appearance of water areas, the bathymetry layer from the Allen Coral Atlas was used as additional guide for the delineation. The Clip Raster tool in ArcGIS Pro was used to extract the image pixels within the ROI polygons. Scatter Plot charts were then created for each visible band, with the NIR band as the x-axis and the visible band as the y-axis. The slope value from the resulting linear regression equation for each band was used as input parameter for the image correction defined in Equation 1. The minimum sample value in the NIR band was derived from the statistics of each clipped raster file.

The Raster Calculator was used to apply the sun glint correction to each of the visible image bands. Prior to this, each band was extracted from the multiband composite image. The deglinted image bands were then stacked as an image composite, resulting in the sun glint corrected image. This sun glint correction procedure, from raster clipping to generation of the deglinted image composite, was replicated for all the image dates used.

2.4 Training and Spectral Separability

Training ROIs for the general benthic classes, namely seagrass, coral, sand, and water were delineated as polygons. To prevent bias in the training step, the same set of training polygons were used in classifying all the images. Ten polygons spatially distributed throughout the image extent were delineated for each class.

The spectral separability of the four classes was inspected by plotting the spectral profile of the class ROI means. The effects of the deglinting procedure on the images was also explored in detail using the spectral profiles, aside from visual inspection of the resulting images. The mean band values within the training ROIs were computed by dissolving the polygons according to class. The three PlanetScope images were used as input rasters in the Sample geoprocessing tool and the pixel value per spectral band for each training class was generated as a table. The spectral plots were then created in Excel using these table of values.

2.5 Image Classification

The classification algorithms used in this study were a combination of traditional and machine learning methods. The ML, RF, and SVM classification methods were implemented for each image, using the same set of training data. The training ROIs were used an input to generate a classifier definition file for each image and each classification method using default values. This was then used as input to the image classification algorithm, together with the image to be classified and the image mask.

Among these methods, ML is the most common traditional classifier, extensively used since the 1970s. ML classifies data by assigning image pixels to the class with highest probability, based on the Bayes theorem. It assumes that the distribution of the dataset is known a priori, which becomes a limitation for non-normal data distribution. In contrast, RF is non-parametric ensemble machine learning algorithm that uses multiple decision trees. It combines the outputs to improve classification performance and increase generalization (Breiman, 2001). SVM, also a non-parametric technique, aims to find an optimal hyperplane to maximize separation of the dataset into the specified classes. Unlike other methods that require a large training dataset, SVM is effective for a small training dataset (Mountrakis et al., 2011). The performance of the different classifiers may vary depending on several factors such as image quality, which was part of this study's assessment.

2.6 Accuracy Assessment

The image classification results were compared with benthic habitat data downloaded from the 2020 Allen Coral Atlas (Fig. 3) and 2020 National Mapping and Resource Information Authority (NAMRIA) Coastal Resource Map (CRM) (Fig. 4). Both reference datasets were used in the cross-tabulation with each classification result. The Allen Coral global dataset (Allen Coral Atlas, 2020) uses PlanetScope images, specifically those dated August 2018 to October 2020 for the Philippines. The benthic zone is classified into 6 classes, namely, 'Coral/Algae', 'Sand', 'Rubble', 'Rock', 'Seagrass', and 'Microalgal Mat'. Meanwhile, the latest 2020 NAMRIA CRM is classified into the general classes 'Corals', 'Mangrove', and 'Seagrass/Seaweeds'.

Although similarities exist between the two datasets, there are also evident differences in terms of extent and type of benthic habitat. The Allen Coral benthic map has seven benthic classes, while the NAMRIA benthic map has three, including mangrove areas. Seagrass and seaweeds are also merged into a single class in the latter map. The classification method also varies between the two, with the former map using machine learning and the latter using image interpretation.

In preparation for the accuracy assessment, the two validation datasets were clipped to the image extent. Some attribute table preprocessing steps were performed to make the layers consistent for comparison. The mangrove class in the NAMRIA CRM was excluded since this was not part of the classified images. Generalizations were made for the Allen Coral benthic data, with the microalgal mats class merged with the seagrass class. Meanwhile, the rubble class was merged with coral and the rock class with the sand class. An integer classvalue field was added to both datasets in preparation for the accuracy assessment. A water class was added to the blank areas of both validation datasets based on the image extent.

Since polygon reference maps were used in validating the image classification, a different approach for checking relative accuracy

https://doi.org/10.5194/isprs-archives-XLIX-B3-2026-1349-2026 | © Author(s) 2026. CC BY 4.0 License.

was applied. Instead of generating the confusion matrix using point samples in ArcGIS Pro, the Tabulate Area tool under Spatial Analyst was used. The matrix resulting from this cross-tabulation was then added as input in Excel to compute for the accuracy metrics. This included the overall accuracy (OA), kappa statistic, producer’s accuracy, and user’s accuracy. In cases when the data being cross-tabulated did not have the same classes, such as the absence of the sand class in the NAMRIA CRM, the unmatched row or column was excluded from the accuracy computations. The reference data areas that overlapped with classified land areas were also excluded from the analysis.

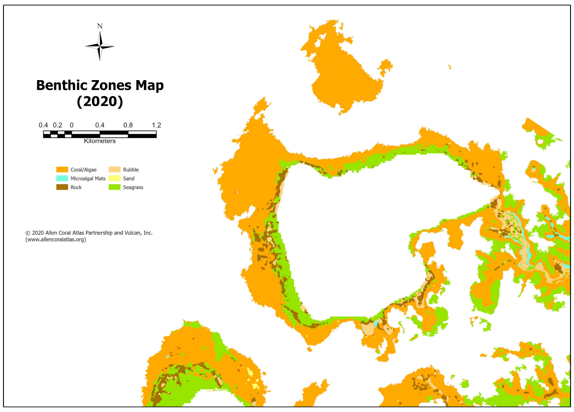

Figure 3. Benthic zones from the Allen Coral Atlas (© 2020 Allen Coral Atlas Partnership and Vulcan, Inc. Available from: www.allencoralatlas.org)

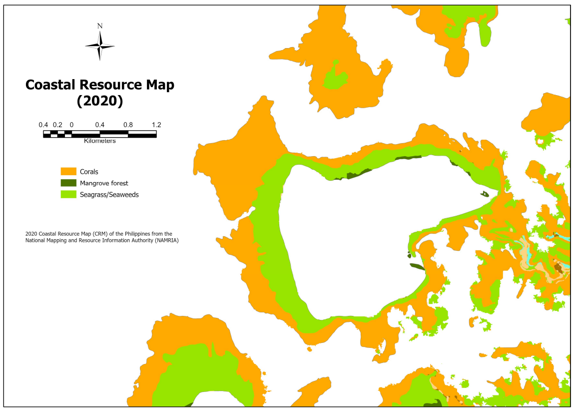

Figure 4. Coastal Resource Map (2020) from the NAMRIA Geoportal. (Credits to: Physiography and Coastal Resource Division, Resource Data Analysis Branch, National Mapping and Resource Information Authority. Available from: https://www.geoportal.gov.ph/)

This was a more direct approach given the available form of the reference data. It also enabled a more complete one-to-one comparison of each pixel in the reference image and the classified image. This method also eliminated the need for preparing the training samples, which will entail several additional steps of data preparation prior to accuracy assessment. It should be noted, however, that the statistics considered as accuracy metrics in this method are not actual accuracies with respect to ground-truth data. The statistics computed from this cross-tabulation indicate the level of agreement or similarity with respect to the reference data. The results from this comparative analysis are only as good as the reference data used. Given the availability of in situ data, an absolute assessment of classification accuracies across the image dates and algorithms may be implemented in future work.

3. Results and Discussion

3.1 Sun Glint Correction

The linear regression computations using the deep-water ROIs yielded the values listed in Table 2. These results indicate the linear relationship between the NIR deep water sample values and the sun glint present in the visible band samples. The linear relationship is strongest and most consistent for the February 16 image, with R^2 values close to 1.0 for all bands. The May 2 image also had high R^2 values, indicating good linear relationship between the two parameters. The application of the sun glint removal method resulted in the following corrected images for the February 16, May 1, and May 2 images (Fig. 5). The corrections were based on each visible band’s linear regression slope with respect to the NIR band. It is evident from these results that the image noise decreased after the correction, leading to more pronounced benthic features. However, the noisy or sun glint features were not completely eliminated after the correction. Moreover, the prominence of the surface waves and other image noise did not seem to have been reduced.

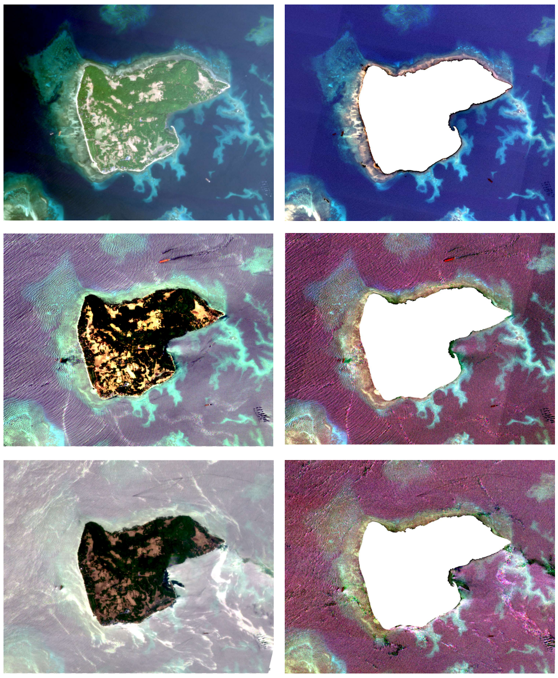

Figure 5. Original and deglinted, masked images for 16 February 2025 (top), 01 May 2025 (middle), and 02 May 2025 (bottom). (Imagery © 2025 Planet Labs PBC)

Date	Band	R^2 value	Slope	NIR_{min}
16 Feb 2025	B1	0.85264861	1.09044513	1
	B2	0.89329774	0.96694023	
	B3	0.91275857	0.98114827	
	B4	0.91425456	0.93721773	
	B5	0.91508586	0.80657603	
	B6	0.91239883	0.70484969	
	B7	0.88825522	0.75377659	
01 May 2025	B1	0.59507587	0.7110813	641
	B2	0.43889783	0.54683122	
	B3	0.57494180	0.7093696	
	B4	0.62237258	0.7390152	
	B5	0.66372860	0.77148789	
	B6	0.49369901	0.61687161	

https://doi.org/10.5194/isprs-archives-XLIX-B3-2026-1349-2026

	B7	0.67500383	0.78405269	
02 May 2025	B1	0.81415800	0.55873945	1764
	B2	0.73585023	0.49809384	
	B3	0.81157265	0.59646143	
	B4	0.85169771	0.67602221	
	B5	0.87926748	0.74167678	
	B6	0.81908299	0.71243237	
	B7	0.88078740	0.79159538	

Table 2. Linear regression parameters for sun glint correction.

3.2 Training and Spectral Separability

The spectral plots provided a quantitative basis for identifying spectral separability of the four benthic classes using each of the three original PlanetScope images. These plots showed which image bands will be useful in distinguishing between the classes. It also gave an indication of the classes that will experience the most confusion due to overlapping or very close pixel values. The findings using these plots were compared with the actual classification results, described in the next section.

It was evident from these results that the February 16 image allowed for the most separability of classes, especially in bands 2, 3, 4 and 5. The May 1 image, meanwhile, did not show good separability between classes except for sand. The overlapping lines for coral and seagrass in this dataset signified that the pixel values of the two classes within the training polygons were not distinguishable from one another. The May 2 image exhibited an unusual behavior, with its almost consistent upward trend towards the longer wavelengths. This may be due to saturation of pixel values owing to the sun glint effect, which was widespread in this image. This was also evident in the overlapping or extremely close lines for coral and water in almost all bands, which indicated that they were not spectrally separable. This may be attributed to sun glint or surface wave noise affecting the signal’s depth penetration. However, compared to the May 1 image, coral and seagrass seemed to exhibit greater and consistent separability in the May 2 image. The coastal blue band (band 1) showed poor separability in all the images.

The effect of the deglinting procedure on the pixel values of the images was also investigated using the spectral plots within the same set of training polygons. The sun glint correction appeared to have a positive effect on the band 1 separability of classes for the February 16 image. However, band 2 experienced the opposite effect, with overlapping lines for seagrass and water. The May 1 deglinted plot showed a very similar pattern to the original image plot. The May 2 plot, despite appearing different from the original image result, also showed an increasing trend towards the NIR band. The sun glint correction did not seem to improve the separability of classes in this particular image, apart from better sand class separability in bands 1 to 4. The other classes, especially the coral and seagrass, became harder to distinguish after the image correction in this particular scenario.

Figure 6 shows the spectral plots for the original and deglinted images. In all the results, whether original or corrected for sun glint, the February 16 image exhibited the best spectral separability for all bands. This was expected as it was the clearest image, enabling the best signal penetration through varying water depths. The spectral plot for this image had the widest range of surface reflectance values between classes, indicating good separability for image classification.

Figure 6. Spectral plots of the original 8-band images (left, from top: February 16, May 1, and May 2) and 7-band deglinted images (right, from top: February 16, May 1, and May 2).

3.3 Image Classification

Three different supervised classification algorithms were compared in this study, based on accuracy metrics, scalability, and ease of use. Training the SVM took noticeably more time than training the ML and RF, with the longest processing time at 2 minutes 59 seconds for the deglinted May 2 image. The training duration increased as the image quality decreased, since finding the optimal hyperplane became more difficult. In the case of both ML and RF training, processing times did not vary across images, taking only 1 to 2 seconds per training. Classification duration for all the algorithms and images did not vary as much, with all scenarios taking less than a minute.

Different image scenarios were classified using the aforementioned algorithms, yielding maps with classes: sand (yellow), coral (orange), seagrass (green), and water (blue). It was evident from initial visual inspection of these classified images that the best results were from the clear February 16 image scene. This yielded the least noisy or speckled classification results for all three methods. Of the three methods used for this image scene, the ML and SVM results using the original images appeared to be the most similar (Fig. 7).

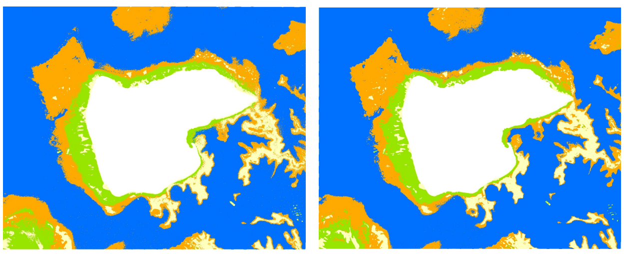

Figure 7. Results for the 16 February 2025 image ML (left) and SVM (right) classifications.

Of the three classification algorithms used, RF resulted in most noise in the classified images. For the clearest February 16 image, the RF classifier also extensively misclassified water areas as coral along the middle portion of the image (Fig. 8). This misclassification was reduced in the 4-band classification result but was still evident. This phenomenon, however, was eliminated in the deglinted classification result. For the May 1 and May 2 images, with widespread surface wave patterns and sun glint, the SVM classifier yielded the least noisy results (Fig. 9). This became most pronounced for the May 2 image results.

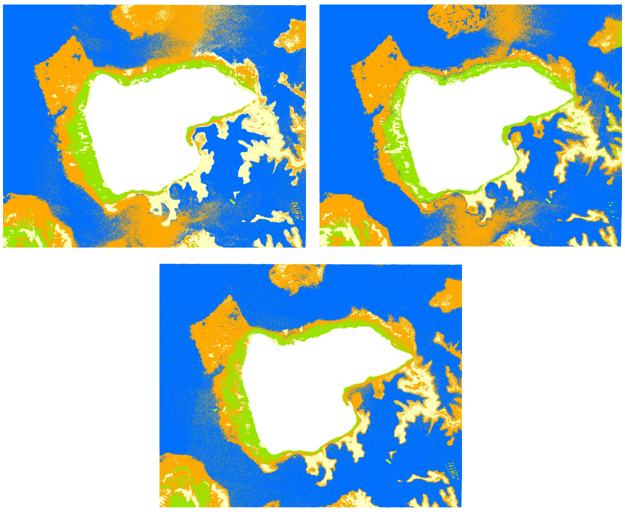

Figure 8. RF classification results for the 8-band (left), 4-band (right), and 7-band deglinted (bottom) 16 February 2025 image.

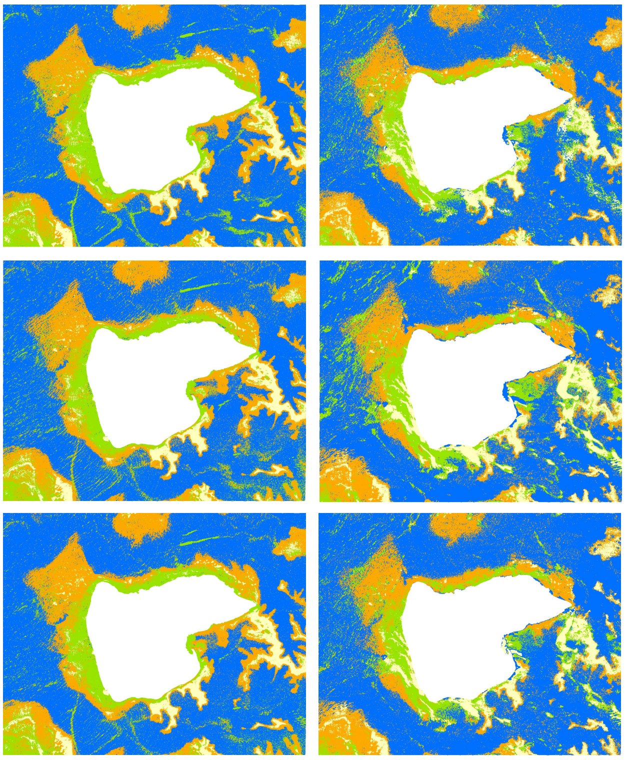

Figure 9. Results for the 8-band original 01 May 2025 (left) and 02 May 2025 (right) images using ML, RF, and SVM (top to bottom).

The effect of sun glint correction on the image classification results was assessed visually and statistically. Upon visual inspection, it appeared that deglinting lessened the classified image noise. However, some seagrass areas in the 8-band and 4-band classification results were classified as sand in the 7-band deglinted classification. The positive result of deglinting was most evident in the May 2 image (Fig. 10), which also had the greatest level of sun glint effect. The water classes misclassified as coral and seagrass in the uncorrected 8-band and 4-band classifications were rectified in the deglinted classification. This was true for all three classification methods, in varying degrees.

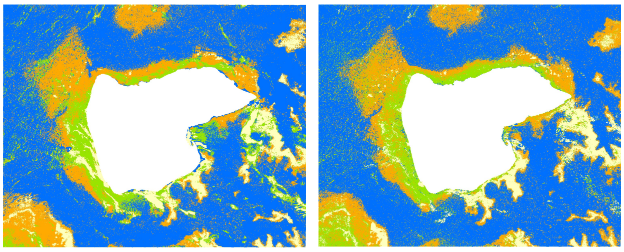

Figure 10. SVM results for 02 May 2025 8-band/original image classification (left) and 7-band deglinted classification (right).

3.4 Accuracy Assessment

Visual analysis of the classification results was further validated using the reference datasets in the cross-tabulation. Overall accuracy and kappa coefficients were computed based on the cross-tabulation results. Overall accuracy shows the number of correctly classified pixels over the total number of pixels, while kappa coefficient is a measure of the agreement between the classification and the reference. The computed accuracy metrics of the 27 image classification results, using the Allen Coral and NAMRIA reference datasets, are shown in Table 3 and 4.

Date	Image	Classifier	OA	Kappa
16 Feb 2025	8-band orig	ML	0.784527	0.592520
		RF	0.658878	0.411611
		SVM	0.799533	0.610691
	4-band	ML	0.796501	0.612042
		RF	0.715077	0.484028
		SVM	0.798462	0.608820
	7-band deglint	ML	0.794548	0.609765
		RF	0.768904	0.562879
		SVM	0.792324	0.597408
01 May 2025	8-band orig	ML	0.727838	0.510999
		RF	0.708162	0.483842
		SVM	0.730632	0.515938
	4-band	ML	0.709922	0.478614
		RF	0.691162	0.457576
		SVM	0.697080	0.465036
	7-band deglint	ML	0.736560	0.522855
		RF	0.734731	0.517841
		SVM	0.729511	0.511630
02 May 2025	8-band orig	ML	0.694650	0.446357
		RF	0.655481	0.395275
		SVM	0.686467	0.428607
	4-band	ML	0.675681	0.422946
		RF	0.646587	0.380981
		SVM	0.655752	0.389123
	7-band deglint	ML	0.712847	0.476860
		RF	0.690408	0.445660
		SVM	0.710689	0.469821

Table 3. Accuracy assessment using Allen Coral reference data.

Date	Image	Classifier	OA	Kappa
16 Feb 2025	8-band orig	ML	0.903148	0.796252
		RF	0.786447	0.577649
		SVM	0.893861	0.771619
	4-band	ML	0.901088	0.789488
		RF	0.797319	0.593750
		SVM	0.888581	0.761653
	7-band deglint	ML	0.898386	0.789059
		RF	0.858556	0.702355
		SVM	0.890489	0.765767
01 May 2025	8-band orig	ML	0.821398	0.657872
		RF	0.787262	0.600276
		SVM	0.819159	0.654295
	4-band	ML	0.790763	0.602025
		RF	0.765425	0.562181
		SVM	0.780241	0.587260
	7-band deglint	ML	0.834945	0.676826
		RF	0.823552	0.658426
		SVM	0.822264	0.659028
02 May 2025	8-band orig	ML	0.775536	0.548806
		RF	0.721571	0.459232
		SVM	0.754516	0.506058
	4-band	ML	0.739881	0.499401
		RF	0.699474	0.427705
		SVM	0.710135	0.444353
	7-band deglint	ML	0.799835	0.600762
		RF	0.779664	0.565465
		SVM	0.801051	0.599923

Table 4. Accuracy assessment using NAMRIA reference data.

The computed accuracy statistics showed that the 8-band SVM classification using the February 16 image (Fig. 11) had the best performance in overall accuracy when compared to the Allen Coral benthic map. It was second in terms of kappa statistic, only marginally lower than the 4-band ML classification for the same image date and reference data. Using the NAMRIA CRM as the reference data, the February 16 8-band image classified using ML (Fig. 12) outperformed the rest of the results for both OA and kappa. The May 2 4-band RF results consistently performed the worse using either of the two reference maps. Based on visual inspection of the classification results, there were non-water pixels that were misclassified as water, most likely due to image noise. An additional contextual editing step to correct these obviously misclassified pixels will lead to higher classification accuracy metrics.

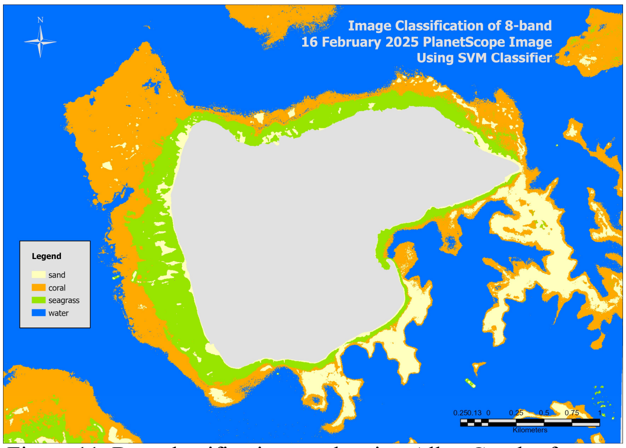

Figure 11. Best classification result using Allen Coral reference data (16 February 2025 8-band image using the SVM classifier).

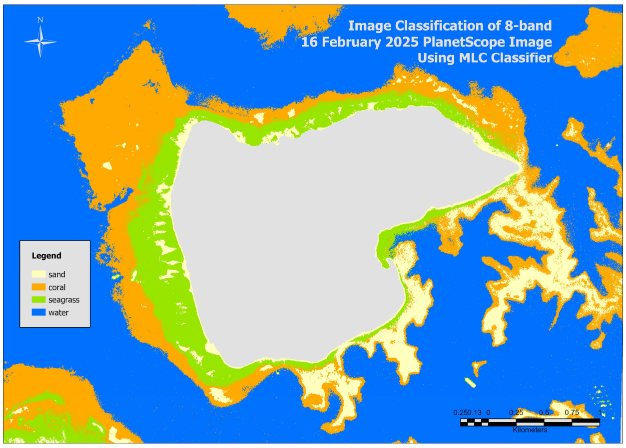

Figure 12. Best classification result using NAMRIA reference data (16 February 2025 8-band image using the ML classifier).

The combined visual inspection and accuracy assessment statistics indicated that the February 16 8-band ML and SVM classifications produced the best results. The 4-band ML classification result for the same data followed closely for both reference data. The 7-band deglinted classifications for the February 16 image also yielded good results that were comparable to the 8-band results. The RF classifier almost consistently had the lowest accuracies across all the scenarios. Overall, the best results using the February 16 image were supported by the previous analysis of the spectral plots, with it having the greatest class separability. The May 2 image, on the other hand, consistently had the worst performance based on visual and statistical results, as supported by the spectral plots. This indicates that image scenes that are very close in acquisition date can have different results, not due to actual habitat change but due to image quality variations. It should be noted, however, that the higher accuracy statistics in the clear image was largely due to water, largely affected by sun glint in the other images.

4. Conclusion

The analysis using the spectral plots, visual inspection of classified images, and accuracy assessment statistics consistently showed that ML and SVM produced the best results. ML, despite being a traditional classifier, had comparable performance as the more sophisticated SVM machine learning algorithm. This may be since only four general benthic classes were used in this study, which had good separability for the clear February 16 image. A possible next step is to perform classification using more detailed benthic classes to verify classifier performance.

Mapping of benthic habitats using remote sensing commonly only use the visible bands since water attenuation effect increases towards longer wavelengths. However, the use of all eight spectral bands of the PlanetScope images resulted in slightly better classification accuracies for the May 1 and May 2 images. The February 16 image classifications, on the other hand, had mixed results for the 8-band and 4-band image band combinations. This seemed to indicate that the additional bands contribute to spectral separability for noisy images, but the 4-band images may be able to suffice for clear images.

The application of the deglinting procedure showed a consistent improvement in accuracy statistics for the RF classifications across all image dates and band combinations, for both reference datasets. However, this classifier also had the lowest overall performance compared to the ML and SVM classifiers. These findings may be further validated for other benthic conditions in other areas or using other datasets. Future research can explore the use of localized or zoned sun glint correction methods to account for variations in glint intensity and possibly improve accuracies. The use of actual training data will also be useful in further validating the findings from this study.

Overall, the analysis and results derived from this study showed the potential of using freely available, high-resolution PlanetScope images for mapping seagrass and general benthic classes. The higher spatial resolutions of such remotely sensed images allow for detection of fragmented benthic habitat. The high temporal resolution increases monitoring frequency and useful image availability, particularly for tropical areas and seasonal habitat. The diverse results even from close acquisition dates, however, imply that careful image selection is needed. Image quality varies widely across acquisition dates, which can significantly impact the classification results.

Nonetheless, the growing accessibility to more satellite image data options and advanced classification algorithms presents significant opportunities for research. Accurately mapping and monitoring ecologically important, highly threatened, spatially complex, and seasonally variable blue carbon ecosystems, such as seagrass habitats, is now made possible with increased image availability. This can pave the way for evidence-based and sustainable conservation strategies, targeting both ecological integrity and human wellbeing.

Acknowledgements

The author is grateful to Planet Labs for providing access to the satellite images used in this study through the Education and Research program.

References

Allen Coral Atlas, 2020. Imagery, maps and monitoring of the world's tropical coral reefs. doi.org/10.5281/zenodo.3833242.

Baumstark, R., Duffey, R., Pu, R., 2016. Mapping seagrass and colonized hard bottom in Springs Coast, Florida using WorldView-2 satellite imagery. *Estuar., Coast. Shelf Sci.*, 181, 83-92. doi.org/10.1016/j.ecss.2016.08.019.

Breiman, L., 2001. Random forests. *Machine Learning*, 45(1), 5-32. doi.org/10.1023/A:1010933404324.

Bremner, J., Petus, C., Dolphin, T., Hawes, J., Beguet, B., Devlin, M.J., 2023. A seagrass mapping toolbox for South Pacific environments. *Remote Sens.*, 15(3), 834. doi.org/10.3390/rs15030834.

Cullen-Unsworth, L., Unsworth, R., 2013: Seagrass meadows, ecosystem services, and sustainability. *Environ. Sci. Policy Sustain. Dev.*, 55(3), 14-28. doi.org/10.1080/00139157.2013.785864.

de Fouw, J., Madden, C.J., Furman, B.T., Hall, M.O., Verstijnen, Y., Holthuijsen, S., Frankovich, T.A., Strazisar, T., Blaha, M., Van Der Heide, T., 2024. Reduced seagrass resilience due to environmental and anthropogenic effects may lead to future die-off events in Florida Bay. *Front. Mar. Sci.*, 11(1366939). doi.org/10.3389/fmars.2024.1366939.

de los Santos, C.B., Olivé, I., Moreira, M., Silva, A., Freitas, C., Luna, R.A., Quental-Ferreira, H., Martins, M., Costa, M.M., Silva, J., Cunha, M.E., Soares, F., Pousão-Ferreira, P., Santos, R., 2020. Seagrass meadows improve inflowing water quality in aquaculture ponds. *Aquaculture*, 528(735502). doi.org/10.1016/j.aquaculture.2020.735502.

Hedley, J.D., Harborne, A.R., Mumby, P.J., 2005. Technical note: Simple and robust removal of sun glint for mapping shallow-water benthos. *Int. J. Remote Sens.*, 26(10), 2107-2112. doi.org/10.1080/01431160500034086.

Hedley, J.D., Roelfsema, C.M., Chollett, I., Harborne, A.R., Heron, S.F., Weeks, S., Skirving, W.J., Strong, A.E., Eakin, C.M., Christensen, T.R.L., Ticzon, V., Bejarano, S., Mumby, P.J., 2016. Remote Sensing of coral reefs for monitoring and management: A review. *Remote Sens.*, 8(2), 118. doi.org/10.3390/rs8020118.

Hossain, M.S., Bujang, J.S., Zakaria, M.H., Hashim, M., 2015. The application of remote sensing to seagrass ecosystems: an overview and future research prospects. *Int. J. Remote Sens.*, 36(1), 61-114. doi.org/10.1080/01431161.2014.990649.

Kutser, T., Hedley, J., Giardino, C., Roelfsema, C., Brando, V.E., 2020. Remote sensing of shallow waters – A 50 year retrospective and future directions. *Remote Sens. Environ.*, 240(111619). doi.org/10.1016/j.rse.2019.111619.

Li, Y., Bai, J., Chen, S., Chen, B., Zhang, Li., 2023. Mapping seagrasses on the basis of Sentinel-2 images under tidal change. *Mar. Environ. Res.*, 185(105880). doi.org/10.1016/j.marenvres.2023.105880.

Mederos-Barrera, A., Marcello, J., Eugenio, F., Hernández, E., 2022. Seagrass mapping using high resolution multispectral satellite imagery: A comparison of water column correction models. *Int. J. Appl. Earth Obs. Geoinf.*, 113(102990). doi.org/10.1016/j.jag.2022.102990.

Mountrakis, G., Im, J., Ogole, C., 2011. Support vector machines in remote sensing: A review. *ISPRS J. Photogramm. Remote Sens.*, 66(3), 247-259. doi.org/10.1016/j.isprsjprs.2010.11.001.

Ondiviela, B., Losada, I.J., Lara, J.L., Maza, M., Galván, C., Bouma, T.J., van Belzen, J., 2014. The role of seagrasses in coastal protection in a changing climate. *Coast. Eng.*, 87, 158-168. doi.org/10.1016/j.coastaleng.2013.11.005.

Planet Labs PBC, 2025. Planet Application Program Interface: In Space for Life on Earth. San Francisco, CA. https://api.planet.com.

Planet Team, 2025. Planet imagery product specifications. Planet Labs PBC. https://assets.planet.com/docs/Planet_Combined_Imagery_Product_Specs_letter_screen.pdf.

Pu, R., Bell, S., 2017: Mapping seagrass coverage and spatial patterns with high spatial resolution IKONOS imagery. *Int. J. Appl. Earth Obs. Geoinf.*, 54, 145-158. doi.org/10.1016/j.jag.2016.09.011.

United Nations Environment Programme, 2020. Out of the blue: The value of seagrasses to the environment and to people. UNEP, Nairobi.

Unsworth, R.K.F., McKenzie, L.J., Collier, C.J., Cullen-Unsworth, L.C., Duarte, C.M., Eklöf, J.S., Jarvis, J.C., Jones, B.L., Nordlund, L.M., 2018. Global challenges for seagrass conservation. *Ambio.*, 48(8), 801-815. doi.org/10.1007/s13280-018-1115-y.

Veettil, B.K., Ward, R.D., Lima, M.D.A.C., Stankovic, M., Hoai, P.N., Quang, N.X., 2020. Opportunities for seagrass research derived from remote sensing: A review of current methods. *Ecol. Indic.*, 117(106560). doi.org/10.1016/j.ecolind.2020.106560.

Waycott, M., Duarte, C.M., Carruthers, T.J., Orth, R.J., Dennison, W.C., Olyarnik, S., Calladine, A., Fourqurean, J.W., Heck, K.L. Jr, Hughes, A.R., Kendrick, G.A., Kenworthy, W.J., Short, F.T., Williams, S.L., 2009. Accelerating loss of seagrasses across the globe threatens coastal ecosystems. *Proc Natl Acad Sci U.S.A.*, 106(30), 12377-81. doi.org/10.1073/pnas.0905620106.

Wicaksono, P., Harahap, S.D., Hafizt, M., Maishella, A., Yuwono, D.M., 2023. Seagrass ecosystem biodiversity mapping in part of Rote Island using multi-generation PlanetScope imagery. *CF*, 2(19). doi.org/10.20517/cf.2023.09.

Wicaksono, P., Lazuardi, W., 2018: Assessment of PlanetScope images for benthic habitat and seagrass species mapping in a complex optically shallow water environment. *Int. J. Remote Sens.*, 39(17), 5739-5765. doi.org/10.1080/01431161.2018.1506951.

Zoffoli, M.L., Gernez, P., Rosa, P., Le Bris, A., Brando, V.E., Barillé, A., Harin, N., Peters, S., Poser, K., Spaias, L., Peralta, G., Barillé, L., 2020. Sentinel-2 remote sensing of *Zostera noltei*-dominated intertidal seagrass meadows. *Remote Sens. Environ.*, 251(112020). doi.org/10.1016/j.rse.2020.112020.